

Article

Not peer-reviewed version

Image Matching Algorithm-Driven Multi-Beam Customized Meta-Device

[Xingshuo Cui](#), Dan Liu, [Borui Wu](#)^{*}, Yueyi Qin, [Guangming Wang](#), Guangzheng Ren, [Tong Cai](#)^{*}

Posted Date: 30 September 2025

doi: 10.20944/preprints202509.2281.v1

Keywords: metasurface; image matching algorithm; multi-beam; optimization design; amplitude-phase modulation



Preprints.org is a free multidisciplinary platform providing preprint service that is dedicated to making early versions of research outputs permanently available and citable. Preprints posted at Preprints.org appear in Web of Science, Crossref, Google Scholar, Scilit, Europe PMC.

Copyright: This open access article is published under a Creative Commons CC BY 4.0 license, which permit the free download, distribution, and reuse, provided that the author and preprint are cited in any reuse.

Disclaimer/Publisher's Note: The statements, opinions, and data contained in all publications are solely those of the individual author(s) and contributor(s) and not of MDPI and/or the editor(s). MDPI and/or the editor(s) disclaim responsibility for any injury to people or property resulting from any ideas, methods, instructions, or products referred to in the content.

Article

Image Matching Algorithm-Driven Multi-Beam Customized Meta-Device

Xingshuo Cui ^{1,†}, Dan Liu ^{2,†}, Borui Wu ^{3,*}, Yueyi Qin ¹, Guangzheng Ren ¹, Guangming Wang ¹ and Tong Cai ^{1,*}

¹ Air and Missile Defense College, Air Force Engineering University, Xi'an, 710051, China

² State Key Laboratory of Modern Optical Instrumentation, the Electromagnetics Academy Zhejiang University, Hangzhou, 310027, China

³ Air Traffic Control and Navigation School, Air Force Engineering University, Xi'an, 710051, China

* Correspondence: wuberry1118@163.com (B.W.); caitong326@sina.cn (T. C.)

† These authors contributed equally.

Abstract

Achieving multi-beam directional manipulation of electromagnetic waves and energy management of each beam has important application value in fields such as satellite communications. Existing methods for realizing multi-beam formation and energy distribution using metasurfaces have problems such as slow optimization speed and low design accuracy. To break through this design bottleneck, a new design paradigm is proposed that introduces the 2D image matching algorithm into the design process of metasurfaces for multi-beam energy management. By using 2D grayscale images to characterize the far-field patterns generated by the metasurface array and the expected multi-beams, a wavefront characterization and matching optimization model driven by 2D grayscale images is established, ultimately achieving the customized design of beam position, intensity, and sidelobe constraints. The fully customized beam metasurface constructed using this method generates multiple y-polarized reflected directional beams under x-polarized wave incidence, and the beam energy distribution ratio can be customized as expected. Both simulation and test results verify the effectiveness of the proposed method. This method provides a new design idea for metasurface devices for multi-beam energy management.

Keywords: metasurface; image matching algorithm; multi-beam; optimization design; amplitude-phase modulation

1. Introduction

As human living environments become more diverse, high-quality ground-based communication are also facing challenges. This is particularly evident in environments with intricate ground conditions, such as dense forests, mountainous regions crisscrossed by gullies, desert and Gobi areas with sparse communication base stations, and buildings plagued by severe electromagnetic interference. Even the complex sea clutter in distant oceans stands as a critical factor impacting communications. Ground-based communication systems [1–3] typically adopt high-power, full-space coverage methods to ensure communication distance and range, often at the cost of increased weight and volume. Satellite communications [4,5], however, relay and retransmit electromagnetic (EM) waves emitted from the ground through space via on-board transponders, addressing communication challenges in complex environments to a certain extent. For on-board equipment, however, payload is the primary consideration, imposing far stricter requirements and constraints on the weight and volume of on-board transponders compared to ground-based transmitters. Consequently, the beams of satellite communication systems must account for multi-directional beam generation and the attendant energy management issues tailored to communication targets [6,7]. Metasurfaces [8–12]-artificial electromagnetic structure-boast both low-profile and

lightweight characteristics, and can achieve exceptional electromagnetic wave manipulation. They thus provide an effective platform for addressing multi-beam directional shaping and energy management in satellite communication systems [13–15].

In traditional approaches, the manipulation of multi-beam EM waves based on metasurfaces often relies on empirical practices or brute-force optimization to determine the required phase and amplitude distribution of metasurface [16–18]. These methods suffer from inherent drawbacks, including low design accuracy and slow optimization process, while failing to effectively achieve precise beam energy allocation or concurrently constrain sidelobe levels. With the escalating demands for intelligence and low power consumption in communication systems, higher requirements are being placed on the efficiency of multi-beam energy management and the precision of beam position control. Traditional methods are increasingly ill-suited to this new trend in terms of time and energy costs, creating an urgent need for novel, rapid design schemes for customized multi-beam devices. Since the generated multi-beams can be expressed in a spherical coordinate system and projected onto a 2D plane consisting of elevation and azimuth angles, the ideal multi-beams corresponding to the desired 2D wavefront [19,20]. This 2D wavefront can be quantitatively characterized as a desired 2D grayscale image through grayscale processing. In practical design, however, there exists a discrepancy between the actual 2D grayscale image corresponding to the multi-beams realized via metasurfaces and the desired 2D grayscale image. This insight inspired the optimization of multi-beam generation meta-device using image matching algorithms. Image matching algorithms refer to find feature-similar images among two or more images based on specific computational rules, and are widely applied in computer vision, pattern recognition, remote sensing detection, and intelligent driving [21–24]. Accordingly, the actual 2D grayscale image corresponding to the array can be calculated using the mapping model from the array's amplitude-phase distribution to the far-field wavefront. The difference between this actual image and the desired image is computed via 2D image matching algorithms, and this difference is employed as the fitness function for the optimization algorithm. This enables accurate and rapid optimization design without the need for additional computational processing.

This work proposes a new method for constructing fully customized multi-beam meta-devices driven by image matching algorithms. Through a rapid optimization process integrating “data-driven+algorithm iteration”, it successfully achieves precise specification of beam position, intensity, and sidelobe constraints. A fully customized five-beam meta-device with varying energy allocations, constructed with amplitude-phase tunable meta-atoms, is employed to validate the proposed method. The process involves first performing grayscale processing on the 2D image of the far-field wavefront of the metasurface array, then establishing an optimization design model for multi-beam energy management meta-device based on 2D image matching algorithms. Ultimately, this realizes a direct correlation between the far-field wavefront effect and the array's amplitude-phase distribution-i.e., a direct mapping of “device function-design parameters”. A prototype of the meta-device finally obtained through this method was fabricated and tested. Experiment results agreeing with expectations, thereby verifying the method's effectiveness. The proposed design scheme breaks through the limitations of traditional far-field pattern description, establishes an image-based functional function and matching optimization system, and provides a novel design approach for far-field pattern shaping.

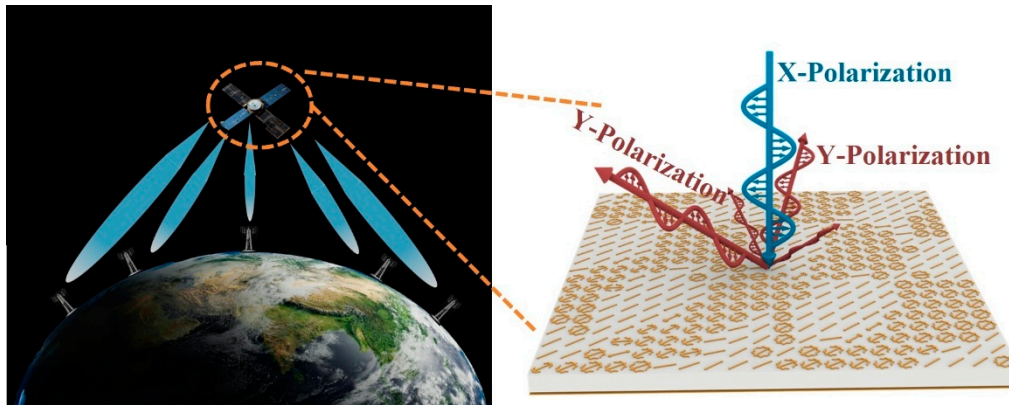


Figure 1. Multi-beam energy management customized meta-device for on-board transponders.

2. Principle and Methods

According to the literature [25,26], the mapping model from the amplitude-phase distribution of the metasurface array to the far-field wavefront of the array $\tilde{F}_{\text{Array}}(\theta, \varphi, \mathbf{l}, \boldsymbol{\alpha}, f)$ can be obtained:

$$\tilde{F}_{\text{Array}}(\theta, \varphi, \mathbf{l}, \boldsymbol{\alpha}, f) = \left| \frac{1}{n^2} \sum_{i=1}^n \sum_{j=1}^n S_{11\text{Cell}}^{\perp}(l_{i,j}, \alpha_{i,j}, f) \exp(-j\Theta) \right| \quad (1a)$$

$$\Theta = \angle S_{11\text{Cell}}^{\perp}(l_{i,j}, \alpha_{i,j}, f) + kp(j-0.5)\sin\theta\cos\varphi + kp(i-0.5)\sin\theta\sin\varphi \quad (1b)$$

wherein, $k = 2\pi/\lambda$, θ and φ are the elevation angle and azimuth angle of the beam, respectively. $S_{11\text{Cell}}^{\perp}(l_{i,j}, \alpha_{i,j}, f)$ is the orthogonally polarized reflection coefficient of the meta-atom, which is related to the meta-atom structural parameters l and α . i and j denote the i -th row and j -th column of the meta-atom in the metasurface array. p is the period of the meta-atom. The above formula indicates that the far-field wavefront model of the multi-beam energy management device is closely related to frequency. In this work, as a verification of the proposed method, only the far-field wavefront at the central frequency of 10 GHz is considered, and the frequency term will be simplified in the subsequent model.

Next, starting from the function of the meta-device for multi-beam energy management, the analytical expression of the device's function "g" is driven, and establish the mapping relationship between the array amplitude-phase distribution and the function g, thereby guiding the rapid optimization design of the device.

According to the analytical expression principle of the function, we can concretely express the grayscale mappings ξ and ζ (from amplitude and phase distribution of the array to the device actual function g, respectively) in the optimization design paradigm model of the amplitude-phase modulation metasurface as follows:

$$g(\mathbf{l}, \boldsymbol{\alpha}) = (\xi \oplus \zeta) \left[\tilde{F}_{\text{Array}}(\theta, \varphi, \mathbf{l}, \boldsymbol{\alpha}) \right]$$

$$= 255 \begin{pmatrix} \tilde{F}_{\text{Array}}(\theta_1, \varphi_1) & \tilde{F}_{\text{Array}}(\theta_1, \varphi_2) & \cdots & \tilde{F}_{\text{Array}}(\theta_1, \varphi_n) \\ \tilde{F}_{\text{Array}}(\theta_2, \varphi_1) & \tilde{F}_{\text{Array}}(\theta_2, \varphi_2) & \cdots & \tilde{F}_{\text{Array}}(\theta_2, \varphi_n) \\ \vdots & \vdots & \ddots & \vdots \\ \tilde{F}_{\text{Array}}(\theta_m, \varphi_1) & \tilde{F}_{\text{Array}}(\theta_m, \varphi_2) & \cdots & \tilde{F}_{\text{Array}}(\theta_m, \varphi_n) \end{pmatrix} \quad (2)$$

For brevity, the meta-atom structure dimensions l and α are omitted from the matrix representation of the above formula. Now, the two-dimensional grayscale processing of the device function in the optimization and design model has been completed.

In satellite communication systems, to maximize energy efficiency, on-board transponders should generate ideal beams directed at the communication targets. These energy beams are expressed in a spherical coordinate system and projected onto a 2D plane consisting of elevation angles and azimuth angles to form the desired 2D wavefront. To quantitatively characterize this 2D wavefront, we perform grayscale processing on the 2D projection, and take a step size of 1° in both the elevation angle and azimuth angle dimensions to generate a 90×359 2D image. The above processing process constitutes the analytical expression of the expected function \tilde{g} of the device:

$$\tilde{g} = \begin{pmatrix} h(\theta_1, \varphi_1) & h(\theta_1, \varphi_2) & \cdots & h(\theta_1, \varphi_n) \\ h(\theta_2, \varphi_1) & h(\theta_2, \varphi_2) & \cdots & h(\theta_2, \varphi_n) \\ \vdots & \vdots & \ddots & \vdots \\ h(\theta_m, \varphi_1) & h(\theta_m, \varphi_2) & \cdots & h(\theta_m, \varphi_n) \end{pmatrix} \begin{cases} m = 90 \\ n = 359 \\ h \in [0, 255] \end{cases} \quad (3)$$

where $h(\theta_1, \varphi_1)$ means the gray value h in direction of (θ_m, φ_n) .

Using binarized grayscale images to characterize the desired spatial multi-beams can more accurately describe the distribution position and intensity of spatial beams, while taking into account the constraints on sidelobe levels in space. In the process of optimizing the array using the heuristic optimization algorithm, the actual 2D grayscale image corresponding to the array can also be calculated based on the mapping model from the array's amplitude-phase distribution to the far-field wavefront. The difference between this actual image and the expected image is computed via the 2D image matching algorithm, and this difference is used as the fitness function of the optimization algorithm. This enables accurate and rapid optimization design without additional computational processing.

In this work, considering the computation time and scale, the Mean Absolute Differences (MAD) algorithm [27] is selected as the image matching algorithm for array optimization, and the index calculation method is as follows [28]:

$$D_{\text{MAD}} = \frac{1}{mn} \sum_{i=1}^m \sum_{j=1}^n |g_{ij} - \tilde{g}_{ij}| \quad (4)$$

wherein, g represents the actual 2D grayscale image calculated from the array amplitude-phase distribution, and \tilde{g} represents the expected image. Taking D_{MAD} as the fitness function of the genetic algorithm, and the setting rules of other parameters of the genetic algorithm remain consistent with those in the previous text. To ensure that the far-field wavefront formed by the array achieves the expected effect, the number of array elements is minimized to realize rapid optimization design. Therefore, a 20×20 element array is adopted in this section. Each element contains two variable parameters: the fractal arm length l and the rotation angle α . Thus, the number of individual DNA loci in the model to be optimized by the genetic algorithm is:

$$N_{\text{DNA}} = 20 \times 20 \times 2 = 800 \quad (5)$$

other parameters of the genetic algorithm are set as follows:

$$\begin{cases} N_{ini} = 200 \\ \varepsilon_G = 10^{-4} \\ N_{GS} = 50 \\ N_{Gmax} = 500 \\ p_C = 0.3 \\ p_M = 0.01 \end{cases} \quad (6)$$

The genetic algorithm-based optimization design model is finally established as follows:

$$\begin{aligned} \min \quad f_{Adapt} = D_{MAD} &= \frac{1}{mn} \sum_{i=1}^m \sum_{j=1}^n |g_{ij}(\mathbf{l}, \boldsymbol{\alpha}) - \tilde{g}_{ij}| \\ \text{s.t.} \quad &\begin{cases} m = 90 \\ n = 359 \\ h \in [0, 255] \\ \alpha \in [10, 85] \\ l \in [1, 6] \end{cases} \end{aligned} \quad (7)$$

Here, as an example, we randomly select five directions (25, -45), (20, 20), (-30, -50), (-25, 30), (0, 0) to generate five beams with random energy allocations (40%, 20%, 20%, 10%, 10%). Then the desired function in formula (3) can be written with the special value conditions in the desired function are as follows:

$$\begin{cases} h(25, -45) = 0.4 \times 255 = 102 \\ h(20, 20) = 0.2 \times 255 = 51 \\ h(-30, -50) = 0.2 \times 255 = 51 \\ h(-25, 30) = 0.1 \times 255 = 25.5 \\ h(0, 0) = 0.1 \times 255 = 25.5 \\ h(\theta_{other}, \varphi_{other}) = 0 \end{cases} \quad (8)$$

wherein, the 2D grayscale values of the desired function for the five directions are consistent with the expected energy ratios.

The corresponding desired grayscale image is shown in Figure 2(a). The desired grayscale image was substituted into the genetic algorithm optimization model[], and the programming implementation was carried out in MATLAB, with the optimization process shown in Figure 2(b). After 495 rounds of survival competition, the change rate of the fitness function was less than the convergence criterion, indicating that the individual had reached the optimal state, i.e., the overall amplitude and phase optimization distribution process for the metasurface array has been completed. The grayscale image of the finally optimized optimal individual is shown in Figure 2(c). Comparing the desired and actual grayscale images, the difference between them is shown in Figure 2(d). The two are in good agreement, with only some errors in the main beam width range. This is because in the algorithm design process, strict restrictions were imposed on the beam width to pursue the accuracy of the designed beam. Thus, even if the beam generated by the actual array becomes wider, it can still be within the allowable range of the desired beam error. The above simulation process verifies the effectiveness of the genetic algorithm optimization.

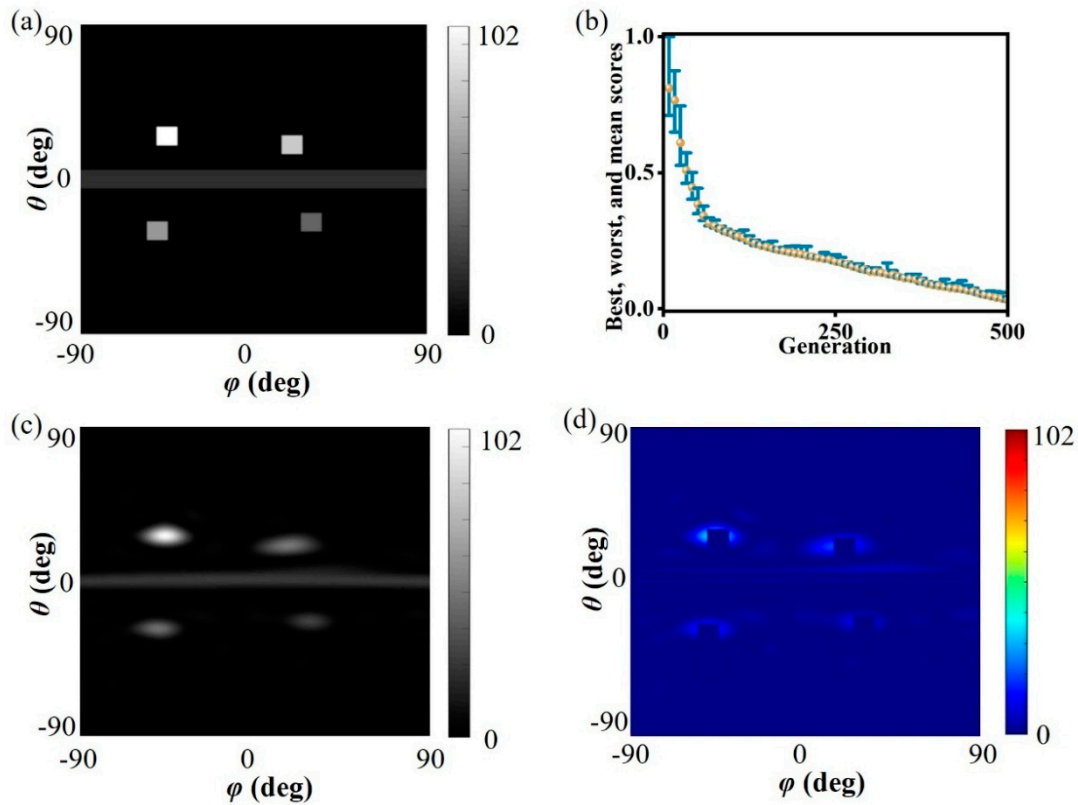


Figure 2. The performance of the optimize algorithm. (a) Desired grayscale image; (b) Genetic algorithm optimization design process; (c) Grayscale image of genetic algorithm optimization result; (d) Difference between desired and optimized grayscale images.

3. Results

After theoretically verifying the accuracy of the proposed two-dimensional grayscale image matching algorithm, the next step is to construct a metasurface based on the optimization results to verify its actual effect, thereby further proving the practicability of the optimization method proposed in this work. The application requirements of multi-beam energy management meta-device have weakened the energy constraints on co-polarized waves and cross-polarized waves, but increased the requirements for decoupling amplitude and phase regulation. Firstly, the mechanism of independent regulation of amplitude and phase by cross-polarization conversion meta-atom is analyzed based on the Jones matrix, details are shown in Section A of supplementary materials (SM). The results as follows:

$$r_{xy} = r_{yx} = e^{j\phi_x} \sin 2\alpha \quad (9)$$

wherein r represents the reflection coefficient and the subscript xy denotes the x -polarized component (i.e., cross-polarized component) reflected or transmitted by the incident y -polarized wave, and the meanings of other subscripts are similar to this. Φ_x represents the reflection phase response of the structure to x -polarized waves in the initial state, Formula (9) shows that the rotating angle of the that metallic structure α can realize the scaling control of the cross-polarized wave amplitude from 0 to 100% when it changes from 0 to 45°. That is, achieve full-range coverage of the cross-polarized wave amplitude regulation. For the reflection phase response of the structure to x and y linearly polarized EM waves illuminates, which are Φ_x and Φ_y respectively, if they meets $\phi_x = \phi_y + 180^\circ$ [12], it is proved in section A of SM that the reflection phase of the cross-polarized wave is only related to the transmission phase Φ_x of the structure under x -polarized wave illumination. Then, 360° full-

range regulation of the reflection phase of the cross-polarized wave can be achieved by adjusting the transmission phase Φ_x under x polarization.

It is worth noting that in Formula (9), the amplitude scaling factor of the cross-polarization response is sine, so this factor is symmetric about $\alpha = 0^\circ$. That is, when $-\alpha$ is taken, it is equivalent to adding a 180° phase to the transmission phase Φ_x . Therefore, in the meta-atom design, it is only necessary to construct a meta-atom whose transmission phase under x polarization covers 180° , which greatly reduces the difficulty of meta-atom design. Next, a reflective amplitude-phase tunable meta-atom with decoupled amplitude and phase is designed based on the above mechanism. The meta-atom is symmetric about both the x -axis and y -axis, make its transmission phase responses to x -polarized and y -polarized waves satisfy a 180° phase difference, and achieve fully decoupled and complete regulation of the amplitude and phase of the cross-polarized reflected wave of the meta-atom by rotating the meta-atom and adjusting the transmission phase of the meta-atom under x polarization to meet the 180° phase coverage. The details of the meta-atom are shown in section B of SM.

After selecting the amplitude-phase tunable meta-atom, parameter scanning simulations were performed to obtain the mapping relationship from structural parameters (l , α) to the amplitude $\Psi(l, \alpha, f)$ and phase $\Phi(l, \alpha, f)$ of reflection coefficient. The concrete expression of the mappings G and H in the optimization design paradigm model of the amplitude-phase modulation metasurface established is completed:

$$\Psi(l, \alpha, f) = G[l, \alpha, f] = |S_{11\text{Cell}}^\perp(l, \alpha, f)| \quad (10a)$$

$$\Phi(l, \alpha, f) = H[l, \alpha, f] = \angle S_{11\text{Cell}}^\perp(l, \alpha, f) \quad (10b)$$

wherein, G and H represent the process of obtaining the reflection coefficient through numerical simulation. Although both the amplitude and phase responses are related to l and α here, the phase is mainly affected by the branch length l , and the amplitude is mainly affected by the rotation angle α . So far, the concrete expression of the mapping relationship at the meta-atom level in the optimization design paradigm model has been completed.

After decoding the optimal individual in previous, the optimized array amplitude-phase distribution is obtained as shown in Figure 3(a)-(b). Then, combining the required amplitude-phase distribution with the amplitude-phase response mapping dataset generated earlier, as shown in Figure S1(d)-(e) of SM, the structural parameters of the amplitude-phase tunable meta-atom designed in this section are obtained as shown in Figure 3(c)-(d).

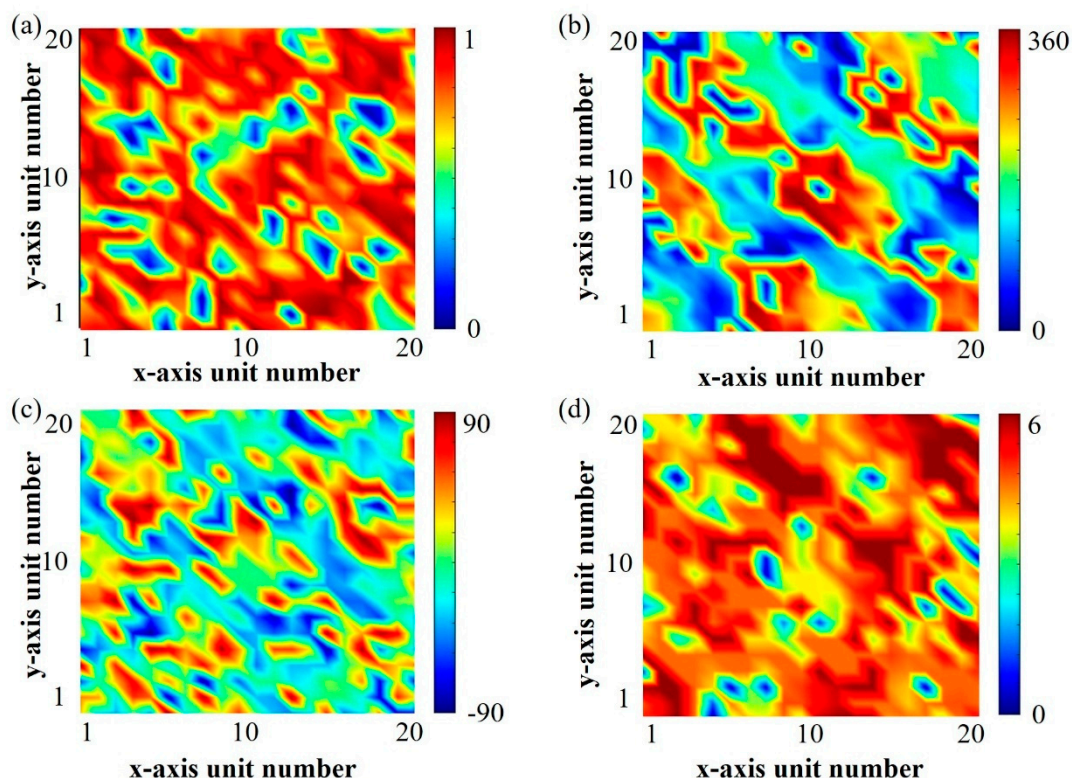


Figure 3. Performance distribution and corresponding meta-atom parameter distribution. (a) Amplitude distribution and (b) phase distribution required after genetic algorithm optimization; (c) Rotation angle α and (d) fractal arm length l required for the corresponding amplitude-phase tunable meta-atom.

Joint modeling and numerical simulation of the array were carried out using MATLAB and CST, and the 3D far-field wavefront was obtained as shown in Figure 4(a). It can be seen from the figure that the metasurface device has multiple beams consistent with the expected directions and meeting the energy distribution conditions. To further show the direction and energy distribution of each beam, we plotted 1D wavefront curves in the azimuth plane where each main beam is located. It should be specially noted that since there may be multiple beams in the same azimuth plane, to avoid misleading caused by the display of far-field wavefronts of different beams, only the far-field wavefront curves in the quadrant where each main beam is located are plotted here, as shown in Figure 4(b). The energy distribution ratio of each main beam is close to the expectation, which again proves that the rapidly optimized metasurface device proposed in this section can realize flexible regulation of the far-field wavefront of the reflected cross-polarized wave. In addition, the 3D far-field pattern is displayed as a 2D far-field pattern shown in Figure 4(c), from which the five designed beams and their energy distribution can also be clearly seen. By comparing the expected 2D grayscale image in Figure 4(a) with the simulated 2D grayscale image in Figure 4(d), it is found that the two are in good agreement, which verifies the effectiveness of the optimization design method for multi-beam energy management metasurfaces based on the 2D image matching algorithm proposed in this section.

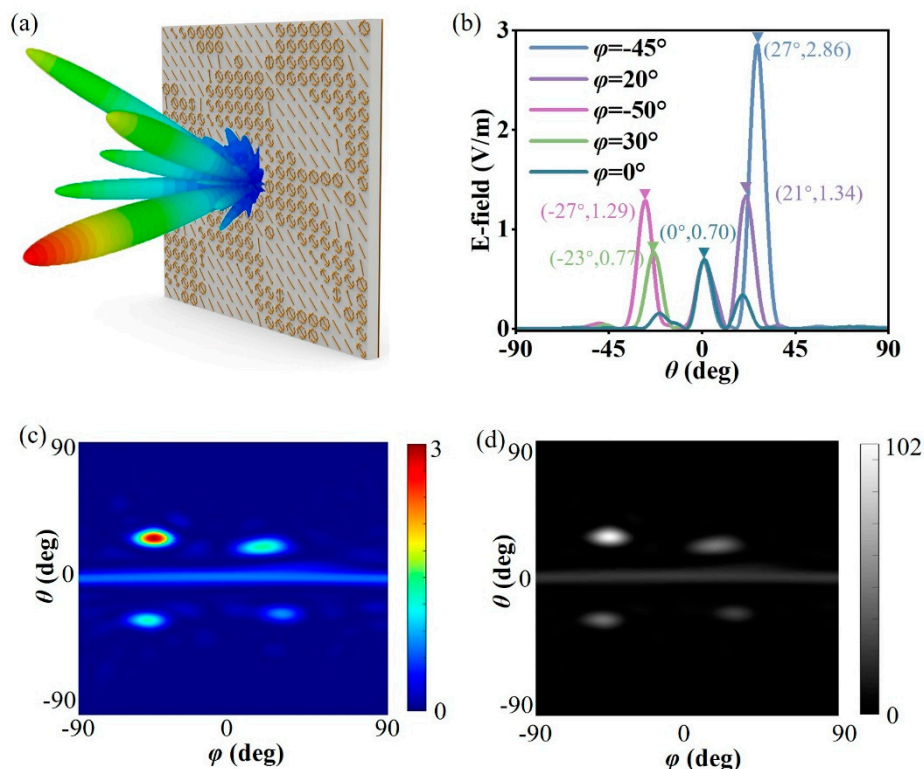


Figure 4. Array modeling and simulation results based on genetic algorithm optimization design. (a) Array modeling and 3D far-field pattern simulation results of genetic algorithm optimization design; (b) Far-field patterns in the planes where each designed beam is located; (c) 2D far-field pattern simulation results; (d) 2D grayscale image corresponding to the simulation results.

To further verify the practical effect of the multi-beam energy management metasurface designed in this section, we fabricated a physical sample and tested it in a microwave anechoic chamber. The physical printed circuit board is double-sided copper-clad, with the designed pattern etched and retained on one side, and separated by an F4B dielectric plate in the middle. The actual photograph is shown in Figure 5(a).

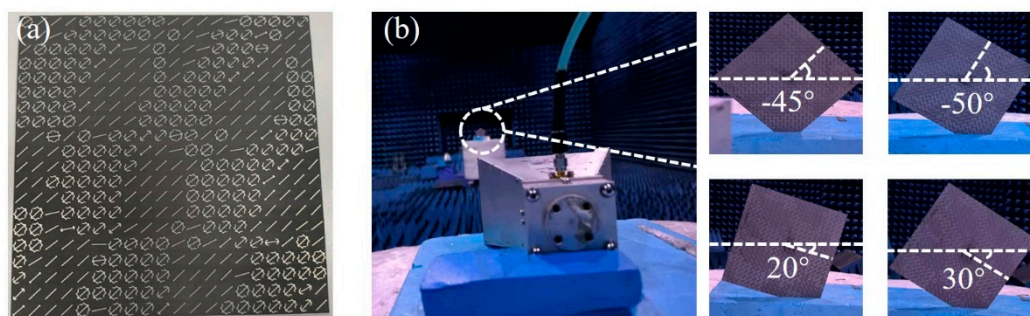


Figure 5. The photograph of the metasurface prototype and test setup. (a) Physical photograph of the multi-beam energy management metasurface prototype; (b) Anechoic chamber test environment. Since the main beams are not located in the xoz or yoz plane, the prototype needs to be placed at an angle.

The actual measurement environment in the anechoic chamber is shown in Figure 5(b). Double-ridged horn antennas are connected to both the input and output ports of the vector network analyzer (Agilent E8362C PNA). The signal receiving horn is mounted on a fixed turntable, and the sample and signal transmitting horn are placed on a remote turntable that meets the far-field conditions.

Since the design in this section is a cross-polarized reflective surface, the receiving horn and the transmitting horn are placed perpendicular to each other. To obtain a more accurate energy distribution of the main beams, the sample needs to be placed rotationally to ensure that the main beams are within the plane of the turntable. However, for the spherical coordinate system decomposition, the main beam at $\theta = 0$ is the same in any φ , so there is no need to place the sample horizontally separately, and it is only necessary to place it at the four angles shown in Figure 5(b). The far-field patterns in the section of each main beam obtained by far-field scanning are shown in Figure 6(a). To intuitively show the peak energy ratio of each beam, we normalized the RCS. The normalized RCS values of the five designed expected beams (25, -45), (20, 20), (-30, -50), (-25, 30), (0, 0) are (0, -3.08, -4.13, -5.38, -5.94) respectively. Figure 6(b) shows the main beam energy ratios under expected, simulated and experimental conditions. It can be seen from the figure that the energy ratios between multiple main beams in the simulation and experiment are consistent with the design expectations, which verifies the effectiveness and accuracy of the optimization design method for multi-beam energy management metasurfaces proposed in this section.

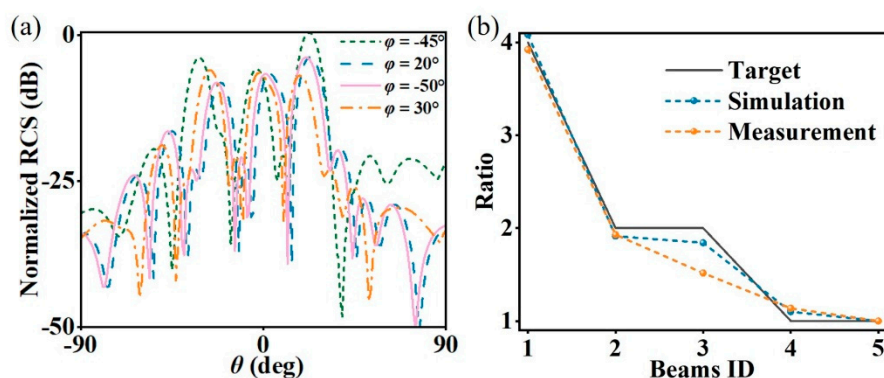


Figure 6. (a) Measured normalized RCS curves of the multi-beam energy management metasurface; (b) Main beam energy ratios.

4. Conclusion

This paper integrates metasurface design with the two-dimensional image matching algorithm in the field of image processing, and establishes a metasurface beam full-customization model that combines beam direction customization and beam energy management. Binary grayscale images are used to characterize the actual multi-beams and the expected spatial multi-beams. The image matching algorithm is employed to calculate the difference between the two, which serves as the basis for array optimization. Finally, a metasurface device capable of generating customized beam directions and energy distributions is obtained. The optimization design method for metasurfaces with multi-beam energy management proposed in this work provides a new design idea for far-field pattern shaping.

Supplementary Materials: The following supporting information can be downloaded at the website of this paper posted on Preprints.org.

Author Contributions: Conceptualization, X. C.; Methodology, X.C. and B.W.; Software, B.W. and D.L.; Formal analysis, X.C. and D.L.; Investigation, Y.Q.; Resources, R.W. and G.R.; Data curation, G.W. and T.C.; Writing—original draft, X.C.; Writing—review & editing, T.C.; Project administration, R.W. and T.C.; Funding acquisition, T.C. All authors have read and agreed to the published version of the manuscript.

Funding: National Natural Science Foundation of China under Grant Nos. 62371467, U24A20224, Shaanxi Provincial Natural Science Basic Research Plan Outstanding Youth Project (Grant No: 2025JC-JCQN-086).

Data Availability Statement: The original contributions presented in this study are included in the article. Further inquiries can be directed to the corresponding authors.

Conflicts of Interest: The authors declare no conflicts of interest.

References

1. Yu, H.; Lee, H.; Jeon, H. What is 5G? Emerging 5G mobile services and network requirements. *Sustainability* **2017**, *9*, 1848.
2. Wang, J. H.; Ling, X. T.; Le, Y. W.; Huang, Y. M.; You, X. H. Blockchain-enabled wireless communications: a new paradigm towards 6G. *Natl. Sci. Rev.* **2021**, *8*, nwab069.
3. Wu, H.; Shao, R.; Xu Z.; Wu, J.-W.; Tan, S.; Wang, X.; Qi, Z.; Cheng, Q.; Zheng, Y.; Luo, Y.; Cui, T.-J. A programmable metasurface antenna that approaches the wireless information mapping limit. *Nat. Electron.* **2025**, *8*, 179-191.
4. Xi, J.; Suo, Z.; Ti, J. The First experimental validation of a communication base station as a ground-based SAR for deformation monitoring. *Remote Sens.* **2025**, *17*, 1129.
5. Abdulkarim, Y.I.; Deng, L.; Awl, H.N.; Muhammadsharif, F.F.; Altintas, O.; Karaaslan, M.; Luo, H. Design of a broadband coplanar waveguide-fed antenna incorporating organic solar cells with 100% Insolation for Ku band satellite communication. *Materials* **2020**, *13*, 142.
6. Tang, X.; Yan, C.; Sun, H.; Meng, L.; He, Y.; Liu, R.; Wang, S.; Wang, L. A high-precision frequency synchronization method based on a novel geostationary communication satellite phase-locked transponder. *Remote Sens.* **2025**, *17*, 1280.
7. Kudsia, C.; Cameron, R.; Tang, W.-C. Innovations in microwave filters and multiplexing networks for communications satellite systems. *IEEE Trans. Microwave Theory Tech.* **1992**, *40*, 1133-1149.
8. Zhao, P.; Ding, X.; Li, C.; Tang, S. Achieving photonic spin hall effect, spin-selective absorption, and beam deflection with a vanadium dioxide metasurface. *Materials* **2023**, *16*, 4259.
9. Jiang, H.; Sheng, L.; Luo, Y.; Meng, L.; Cao, W. Design of tunable broadband graphene-based metasurface with amplitude-phase modulation. *Materials* **2023**, *16*, 4633.
10. Wang, D.; Cui, X.; Liu, D.; Zou, X.; Wang, G.; Zheng, B.; Cai, T. Multi-characteristic integrated ultra-wideband frequency selective rasorber. *Prog. Electromagn. Res.* **2024**, *179*, 49-59.
11. Cai, T.; Zhong, Y.; Liu, D.; Huang, H.; Wang, D.; Yang, Y.; Chen, H.; Lin, X. Observation of polarization-maintaining near-field directionality. *Prog. Electromagn. Res.* **2024**, *181*, 35-41.
12. Cui, X.; Liu, D.; Wang, Z.; Wang, D.; Wu, B.; Wang, G.; Zheng, B.; Cai, T. Wideband and high-efficiency spin-locked achromatic meta-device. *Nanophotonics* **2023**, *12*, 119-127.
13. Wang, C.; Xu, H.-X.; Hu, G.; Liu Y.; Liu, T.; Wang, K.; Zhang, F.; Xu, S.; Xu, J.; Pang, Z. Full-space spin-decoupled versatile wavefront manipulations using non-interleaved metasurface. *Nanophotonics* **2023**, *12*, 3149-3158.
14. Macro, D. R.; Alessio, Z.; Merouane, D.; Mohamed, S. A.; Yuen C.; Rosny, J.; Tretyakov, S. Smart radio environments empowered by reconfigurable intelligent surfaces: how it works, state of research, and road ahead. *IEEE J. Sel. Areas. Commun.* **2020**, *38*, 2450-2525.
15. Sievenpiper, D.F.; Schaffner, J.H.; Song, H.J.; Loo, R.Y.; Tansonan, G. Two-dimensional beam steering using an electrically tunable impedance surface. *IEEE Trans. Antennas Propag.* **2003**, *51*, 2713-2722.
16. Bai, X.; Tan, S.; Mikki, S.; Li, E.; Cui, T.-J. Information-theoretic measures for reconfigurable metasurface-enabled direct digital modulation systems: an electromagnetic perspective. *Prog. Electromagn. Res.* **2024**, *179*, 1-18.
17. Liang J.-C.; Zhang, L.; Luo, Z.; Jiang, R.-Z.; Zhang W.-C.; Wang, S.-R.; Sun, M.-K.; Jin, S.; Cheng, Q.; Cui, T.-J. A filtering reconfigurable intelligent surface for interference-free wireless communications. *Nat. Commun.* **2024**, *15*, 3838.
18. Zhang, M.; Yao, S.; Zhu, B.; Lin, J.; Tao, J.; Shang, W.; Zhang, W. Movable typography inspired tunable meta-cylinder for multi-directional microwave beam shaping. *Adv. Mater. Technol.* **2024**, *9*, 2302108.
19. Zhuo, Y.; Mao, T.; Li, H.; Sun, C.; Wang, Z.; Han, Z.; Chen, S. Multi-beam integrated sensing and communication: state-of-the-art, challenges and opportunities. *IEEE Commun. Mag.* **2024**, *62*, 90-96.
20. Shen, D.; Dai, L.; Su, X.; Suo, S. Multi-beam design for near-field extremely large-scale RIS-aided wireless communications. *IEEE Trans. on Green Commun. Netw.* **2023**, *7*, 1542-1553.

21. Zhu, H.; Zhao, Y. G.; Fast image correlative matching based on genetic algorithm. *J. Infrared Millimeter Waves* **1999**, *18*, 145-150.
22. Yue, G.; Xu, Y. An area based image matching algorithm and its implementation. *2012 Third World Congress on Software Engineering* **2012**, 147-150.
23. Zhang, X.; Feng, Z. New development of the image matching algorithm. *Ninth International Conference on Graphic and Image Processing (ICGIP 2017)* **2018**, 106151T.
24. Kazmer, D.O.; Olanrewaju, R.H.; Elbert, D.C.; Nguyen, T.D. Design of shape forming elements for architected composites via bayesian optimization and genetic algorithms: a concept evaluation. *Materials* **2024**, *17*, 5339.
25. Wu, B.; Liu, T.; Wang, G.; Cui, X.; Jia, Y.; Wang, Y.; Zhai, H. Integrated electromagnetic sensing system based on a deep-neural-network-intervened genetic algorithm. *Photon. Res.* **2025**, *13*, 387-394.
26. Zhang, H.; Zhang, L.; Liu, S.; Mao, Z.; Ma, Y.; He, P.-H.; Cui, W.-Y.; Huang, Y.-F.; Yang, Q.; Cui, T.-J. Measurement of time-range-angle-dependent beam patterns of frequency diverse arrays. *Prog. Electromagn. Res.* **2024**, *180*, 13-24.
27. Feng, N.; Wang, H.; Wang, X.; Zhang, Y.; Qian, C.; Huang, Z.; Chen, H. Highly accurate and efficient 3D implementations empowered by deep neural network for 2DLMs-based metamaterials. *Prog. Electromagn. Res.* **2024**, *180*, 1-11.
28. Cui, X.; Wang, G.; Wang, D.; Li, X.; Cai, T.; Liu, K. Ultra-broadband transmissive gradient metasurface based on the topologically coding optimization method. *Opt. Express* **2021**, *29*, 22136-22145.

Disclaimer/Publisher's Note: The statements, opinions and data contained in all publications are solely those of the individual author(s) and contributor(s) and not of MDPI and/or the editor(s). MDPI and/or the editor(s) disclaim responsibility for any injury to people or property resulting from any ideas, methods, instructions or products referred to in the content.